Electronic structure characterization by photoelectron spectroscopy of $BaZrS_3$ perovskite powder and thin film

Stefania Riva[1], Soham Mukherjee[1], Sergei M. Butorin[1], Corrado Comparotto[2], Garima Aggarwal[2,†], Abdel Rahman Allan[3], Evelyn Johannesson[1,4], Mahmoud Abdel-Hafiez[3,1,], Jonathan Scragg[2], Håkan Rensmo[1,4,*]*

[1,]Department of Physics and Astronomy, Molecular and Condensed Matter Physics, Uppsala University Box 516, SE-75120 Uppsala, Sweden*

[2]Division of Solar Cell Technology, Department of Materials Science and Engineering, Uppsala University, Uppsala 75237, Sweden

[3]Department of Applied Physics and Astronomy, University of Sharjah, P. O. Box 27272 Sharjah, United Arab Emirates

[4]Wallenberg Initiative Materials Science for Sustainability (WISE), Uppsala University Box 516, SE-75120 Uppsala, Sweden

Abstract

Chalcogenide perovskites exhibit optoelectronic properties that position them as breakthrough materials in the field of photovoltaics. We report a detailed investigation into the electronic structure and chemical properties (XPS) of polycrystalline $BaZrS_3$ perovskite powder, complemented by an analysis of their geometric atomic arrangement using XRD and XAS. The results are compared with measurements on sputtered polycrystalline $BaZrS_3$ thin film prepared through rapid thermal processing. Moreover, we establish a correlation between the experimental valence band spectra and the theoretical density of states derived from DFT calculations, thereby discerning the orbital constituents involved. While bulk characterization confirms the good quality of the powder, depth-profiling achieved by photoelectron spectroscopy utilizing Al K_α (1.487 keV) and Ga K_α (9.25 keV) radiations shows that, regardless of the fabrication method, the oxidation effects extend beyond 10 nm from the sample surface, with specifically zirconium oxides occurring deeper than the oxidized sulfur species. The hard X-ray photoelectron spectroscopy study on the powder and thin film detects signals with minimal contamination contributions and allows the determination of the valence band maximum position with respect to the Fermi level. Our analysis gives an improved understanding of the electronic structure of $BaZrS_3$, linking the electronic structure

of this semiconductor to the fundamental bonding properties of the material, providing knowledge which is crucial for interfaces development, and consequently, for device integration.

Introduction

The term perovskite refers to a class of compounds with the chemical formula ABX_3, where A and B represent the cations with oxidation state II and IV, respectively, and X denotes the divalent anion. A notable subgroup within this category is the chalcogenide perovskites, where the cation candidates with oxidation state II include Ba, Sr, Ca, Eu; the cation with oxidation state IV is either Zr or Hf, while the halide X may be either S and/or Se. Among all the combinations, $BaZrS_3$ emerges as one of the most promising compounds for applications in terms of phase stability against air, moisture and high pressure [1–3], abundance of elements in the Earth's crust and safety considerations[4]. Crystalline $BaZrS_3$ assumes a distorted orthorhombic structure, where the Ba^{2+} cations are embedded in cuboctahedral voids of corner-shared octahedrals units of ZrS_6, with a cooperative tilt of 12.2 degrees[2]. In terms of the optical properties, the $BaZrS_3$ bandgap is between 1.7 and 1.8 eV, and its absorption coefficient is > 10^5 cm^{-1} [3,5], making it suitable for photovoltaic applications in a tandem structure[6].

To-date, the scientific community has devoted considerable efforts into synthesizing stoichiometric $BaZrS_3$ thin films at low temperatures using various fabrication methods, such as sputtering[7,8], molecular beam epitaxy[9], pulsed laser deposition[5] and bulk solid state methods[10]. X-ray diffraction (XRD) confirms the successful synthesis of $BaZrS_3$, yet observations indicate a partial replacement of S with O atoms[11], or/and the possible formation of ZrO_2[12]. Although stoichiometric bulk samples of $BaZrS_3$ have been successfully synthesised, demonstrating resistance to bulk oxidation even at high temperature[1], the oxyphilic nature of the constituent elements, particularly Zr, appears to result in some surface oxidation. The oxidation may occur through direct air exposure or during synthesis itself, in either case modifying the surface chemistry. In this regard, TEM imaging showed an off-stoichiometric composition in the topmost few nanometers [9,12]. The investigation of the $BaZrS_3$ surface is a key factor for understanding the behaviour of the material in a device context, where the

electronic structure and interfacial energetics are important for the extraction of charge carriers.

X-ray photoelectron spectroscopy (XPS) is a non-destructive surface sensitive technique with maximum probing depth of 15 nm, which can help in understanding the electronic structure, chemical composition and electron dynamics occurring at the surfaces and buried interfaces. The use of different photon energies permits to distinguish chemical species at different depths. Furthermore, XPS allows for determination of the position of the valence band maximum with respect to the Fermi level, which is crucial for constructing energy levels diagrams when combining $BaZrS_3$ with other materials in devices[13,14]. Additionally, it is possible to probe experimentally the density of states (DOS) at the occupied valence band. DOS calculations on $BaZrS_3$ in the $GdFeO_3$-type perovskite structure reveal the valence band to be composed mainly by high-density states of S 3p and Zr 4d, while the main conduction band states are S 3d, Ba 5d and Zr 4d[6,15,16]. Comparison between direct mapping of experimentally measured DOS to theoretically calculated element-specific contributions is difficult to achieve and experimental values of the valence band maximum (VBM) are of interest for the evaluation of the materials' candidacy for forming a junction.

In this work, polycrystalline $BaZrS_3$ samples in powder and thin film forms were investigated. XPS measurements for the powder were acquired at two photon energies: soft X-rays (Al K_α, 1.487 keV) and hard X-rays (Ga K_α, 9.25 keV), allowing us to perform depth-profiling of the sample, while a comparison between the powder and the thin film is reported when measured at the same high photon energy (9.25 keV). Moreover, the valence band of the samples were compared to DFT calculations, identifying the different orbital components and how their contributions are related to the distorted orthorhombic geometry, as well as evaluating the value of the VBM. The present paper aims to serve as a reference for future spectroscopy studies on the interface and electronic structure of $BaZrS_3$, which may help the interfacial control, an important factor for the design of devices.

Methods/Experimental section

Synthesis of powder and characterization. All preparation steps of weighing, mixing, grinding, and storage were conducted inside an argon-filled glove box, with oxygen (O_2) and water (H_2O) levels maintained at less than 0.1 ppm. The powder of $BaZrS_3$ was synthesized within an

evacuated silica-glass ampoule[17] using pure elements: Ba (0.5 mm granules, Merck, 99.9%), Zr powder (99.5%), and S powder (Labtex, 99.5%). The elements were precisely weighted in an atomic ratio of 1:1:3 and carefully sealed in a quartz ampoule. Subsequently, the ampoule was evacuated and sealed before being placed in a horizontal tube furnace. The temperature was gradually increased to 750 °C over several weeks. The outcome of this process was a mixture of barium and zirconium sulfides, with no traces of elemental sulfur detected. To obtain the final product of $BaZrS_3$, the substance was then ground in an inert atmosphere and transferred to another quartz glass ampoule. Following this, it went through annealing for several weeks at 750 °C, facilitating further structural development and refinement. This multistep synthesis process aimed to ensure the purity and stability of the $BaZrS_3$ powder. Structural properties of the obtained $BaZrS_3$ powder sample were analyzed by X-Ray Diffraction (XRD) (model: Bruker D8) with Cu K_α radiation (1.4506 Å), allowing the determination of the lattice constants of the unit cell.

Synthesis of thin film and characterization. The thin film was prepared on a silicon substrate via sputtering from BaS and Zr target in an atmosphere of H_2S and Ar, with a consequent annealing process at 900 °C, as described in our previous report[7]. The sample was defined as the best of a temperature annealing series in terms photoluminescence peak, XRD analysis, XAS and XPS characterization [7,18].

X-ray absorption spectroscopy (XAS). The Zr K-edge for $BaZrS_3$ powder was measured by XAS at the Deutsches Elektronen-Synchrotron DESY (Hamburg, Germany) at the beamline P64[19], Hamburg, using high photon flux ($\sim 10^{12}$ photons/s) on the sample and high resolution ($\delta E/E \approx 10^{-4}$). The incoming photon beam was monochromatized through a Si (111) double crystal monochromator. N_2 gas was used in the ion chambers to absorb ~5 % of the flux, and an identical set up was used for the transmission and the reference channels, with the later one hosting Zr metal foil to account for any energy offsets. The powder was mixed with boron nitride and calculated for an edge jump of ~ 1.5, pressed into pellets, placed on Kapton tape, and mounted at 45° to the incoming X-ray beam, allowing simultaneous measurements in transmission and fluorescence geometry. A PIPS detector was used to collect the fluorescence data. The XAS data were collected to achieve good statistics up to ~ 1000 eV beyond the Zr edge position, which translates to wavenumbers as high as ~ 16 $Å^{-1}$. The corresponding Zr K-XAS measurements on the sputtered thin films of $BaZrS_3$ were performed at the BALDER

beamline, as reported previously[18]. All XAS data sets were processed and analyzed using Athena-Artemis software suite, a front end to FEFF and IFEFFIT.[20] The subtracted background was calculated using AUTOBK algorithm implemented in the software.[21] The errors were estimated by a standard Levenberg-Marquardt, non-linear minimization of the statistical χ^2 parameter, built within the FEFF program. Fits to all Zr in R (real part and magnitude) and q-spaces, extracted EXAFS parameters and their associated error limits are detailed in the Supporting Information.

X-ray photoelectron spectroscopy. XPS measurements were performed at the Kai-Siegbahn laboratory at Uppsala University. The laboratory is provided with two monochromatic photon sources, Al K_α (1.487 keV) and Ga K_α (9.25 keV), and a Scientia EW4000 spectrometer. For the characterization of the $BaZrS_3$ powder, both sources were exploited to get a depth profile view. Given the challenge with poor conductivity of the powder, these were spread and pressed on a soft indium foil that was mounted on a metal sample holder. To ensure neutralization, the low (Al K_α) and high (Ga K_α) photon energy measurements for the powder were performed with the aid of a flood gun with an ion energy in the range of respectively about 0.5 V and 3.65 V and an emission current of 8 μA. During the measurements the base pressure of the main chamber was kept at $\sim 10^{-10}$ mbar. All the surveys and high photon energy spectra were collected in sweep mode with a pass energy of 500 eV, while the spectra measured with Al K_α radiation were collected with a pass energy of 200 eV. For the core levels spectra, the energy step was 0.1 eV and dwell time was fixed at 96 or 123 ms, while for the survey spectra the energy step was 0.5 eV and the dwell time 96 ms. To isolate the contribution of the perovskite in the valence band of the powder at Al K_α, we performed a subtraction of valence bands of $BaZrS_3$ from the In foil, measured with the same pass energy, dwell time and energy step size. Before subtraction, the energy calibration and intensity normalization were performed using the In 3d peaks. The fits of the peaks were performed considering a combination of Shirley and linear background, and the peaks positions and widths were found following the least square approximation method. The thin film S $2p_{3/2}$ core level peak assigned to $BaZrS_3$ was measured at 161.15 eV vs Fermi. All other samples were energy calibrated by aligning the $BaZrS_3$ S $2p_{3/2}$ core level peaks to this value, i.e. by setting $BaZrS_3$ S $2p_{3/2}$ peak position to 161.15 eV.

The $BaZrS_3$ thin film sample was mounted in the XPS system using carbon tape and no charging was observed. All the spectra were collected in sweep mode and the dwell time was 96 ms. The survey was measured with 500 eV pass energy and 0.5 eV energy step size, while the core levels spectra were collected with pass energy of 300 eV and energy step 0.1 eV. For all the thin film measurements, Au $4f_{7/2}$ was employed for the energy calibration, while intensity was divided by the number of sweeps or normalized to enable a comparison with the other measurements. As calculated from the pass energy E_p, the broadening of the peaks due to the instrumentation is 0.4 eV for E_p = 200 eV, 0.6 eV for E_p = 300 eV and 1.0 eV for E_p = 500 eV.

Elemental analysis based on the XPS measurements was performed from the integrated area of the peaks normalized by the number of sweeps and by considering the cross section of the core levels with respect to the incident photon energy (more information about the cross sections of the core levels of interest at 1.487 keV and 9.25 keV are reported in the Supplementary Information).

Calculation methods. For the density functional calculations, the Quantum Espresso v6.8 code[22] was used. The calculations were performed in the full-relativistic mode. In the first round, the exchange-correlation potential was in the form of Perdew, Burke, and Ernzerhof (PBE)[23]. The band structure was calculated in the generalized gradient approximation (GGA). In the second round, GGA exchange functional by Armiento and Kümmel (AK13)[24] (as it is defined in the Libxc v5.1.6 library[25]) without correlation part was used instead of the PBE functional. The full-relativistic norm-conserving PBE pseudopotentials for sulfur, zirconium and barium were generated by the code of the ONCVPSP v4.0.1 package[26] using the input files from the SG15 database[27]. The valence configurations defined in the pseudopotential input files were as $3s^2 3s^4$ for S, $4s^2 4p^6 5s^2 4d^2$ for Zr and $5s^2 5p^6 5d^1 6s^1$ for Ba. The plane-wave cut-off energy was set to 50 Ry. The convergence threshold for density was 1.0×10^{-12} Ry. The Brillouin zone was sampled by an 8x6x8 *k*-point mesh using the Monkhorst-Pack scheme[28]. The calculations were performed for the experimental structure of $BaZrS_3$[29] without the relaxation procedure.

The size of the calculated band gap of $BaZrS_3$ using the PBE functional was found to be 1.16 eV while for the AK13 functional it was 1.81 eV, the latter being in good agreement with experimental measurements[6,7,30,31]. Furthermore, the energy positions of the shallow core

levels calculated using the AK13 functional were also in better agreement with the experiments. Therefore, the results obtained with the AK13 functional are reported in our paper.

Results and Discussion

Morphology and Crystal structure

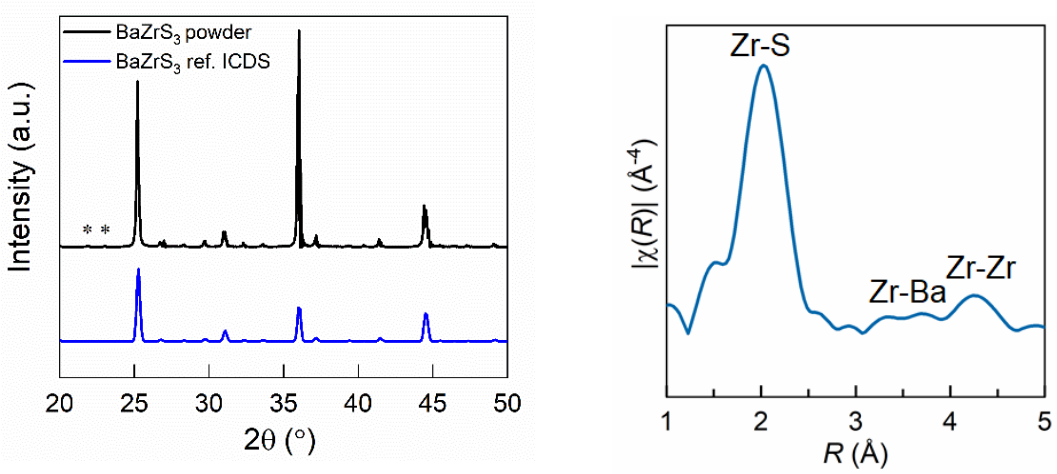

Figure 1. Bulk analyses of the $BaZrS_3$ powder. (a) XRD pattern of $BaZrS_3$ powder compared to a reference profile of orthorhombic $BaZrS_3$; (b) Geometric distribution of the near neighbors around a central Zr as modulus of χ(R), obtained by the EXAFS characterization.

The SEM analysis performed on the powder revealed the crystal dimensions to be from tens to hundreds of µm (SEM image is in Fig. S1b in Supplementary Information), and the corresponding EDX showed a perovskite formula unit of: 22 % Ba, 20 % Zr, 50 % S and 8% O, which indicates a slightly sulfur-poor composition with a minor oxygen contamination, commonly reported in thermal synthesis techniques. [7,8,12,32,33]

In Fig. 1a, we compare the XRD profile of $BaZrS_3$ powder to the reported reference $BaZrS_3$. The figure shows a clear matching of the prominent Bragg peak positions, namely 2θ = 25.2°, 31.0°, 36.0° and 44.4°, proving the successful formation of the crystalline $BaZrS_3$. These reflections can be indexed to [121], [220], [040] and [042] planes, respectively, characteristic to *Pnma* symmetry observed for the $BaZrS_3$ powder. We notice minor additional peaks "*" (2θ = 21.9° and 23.0°) which can most likely be assigned to Ba-S-O compounds, and not to Ruddleson-Popper phases. Considering the sub-stoichiometry of S in $BaZrS_3$ powder and the correspondence between the XRD $BaZrS_3$ reference profile and the data, it can be deduced

that these contributions are impurities related to undesired surface oxidation, instead of originating from e.g., $BaZrS_3$-$BaZrO_3$ alloys. Since the space group *Pnma* is orthorhombic with the lattice constants $a \neq b \neq c$, one needs to combine Bragg's law and multiple reflections from the XRD profiles to independently estimate the values of *a*, *b* and *c*. Using the three major reflections, [121], [220] and [040], we arrive at the lattice constants of: $a = 7.0533$ Å, $b = 9.9725$ Å, $c = 7.0730$ Å, which are well in agreement with the values reported by literature.[34] Further employing the Debye-Scherrer's law for the [121] reflection (the FWHM of the XRD peak is inversely dependent on the grain size), we find the crystallite sizes to be around 43 nm. A similar analysis of the $BaZrS_3$ thin films yield unit cell dimensions of $a = 7.0511$ Å, $b = 9.9569$ Å, $c = 7.0479$ Å, rather similar to the unit cell dimensions of the powder sample, but a smaller average crystallite size of ~22 nm as already reported[7]. For the details about the polycrystalline thin film, we refer to the papers [7,18]. The powder and thin films of $BaZrS_3$, although grown using very different synthesis strategies, achieves the same orthorhombic structure with rather comparable unit cell dimensions, suggesting the orthorhombic structure to be energetically favored over other higher symmetry perovskite structures. The duration of the thermal process, i.e., 1 minute for the thin films, and several weeks for the powder, respectively, does not seem to have a major impact on the lattice dimensions. It mainly affects the grain growth, forming significantly larger grains for powder (>10 µm qualitatively shown by the SEM image in Fig. S1b in the Supporting Information) compared to thin films (~ 100

nm), as evidenced by electron microscopy analyses[7]. Such large difference in grain sizes, surprisingly enough, is not reflected in our XRD data, where we observe comparable FWHM of the Bragg peaks for the powder and thin films, leading to comparable crystallite sizes (reported in Tab. 1). Our XRD analyses reveal that the average crystallite size for powder (~43 nm) grown by prolonged thermal treatment is indeed, only slightly larger compared to the thin films (~ 22 nm) grown by rapid thermal processing.

Table 1 compiles the morphological and geometric structure information for the powder in terms of crystallite sizes, unit cell dimensions, Zr-S-Zr interatomic distances, Zr-S-Zr bond angles and Zr-S disorder (σ^2), and compares it to the reported parameters for thin film[18]. From Zr K-edge XAS measurements it is possible to extract the modulus of $\chi(R)$, which illustrates the geometric distribution of the near neighbors around a central Zr in real space. For the powder, our EXAFS data analysis yields average Zr-S bond distances ~2.54 Å, two sets of Zr-Ba interatomic distances ranging from 4.08 – 4.39 Å, and Zr-Zr interatomic distances of 4.84 Å (Tab. S1 in the Supplementary Information). Employing a dominant multiple scattering path and validated by perovskite geometry considerations, we calculate the average Zr-S-Zr bond angle to be 144.6°. The extracted pseudo-Debye-Waller factor (σ^2), which account for the

Table 1: Comparison of the powder and thin film with respect to: the average crystallite sizes obtained from segmented fits to the Bragg reflections at [121] and the lattice parameters; the relative atomic distance Zr-S calculated by EXAFS, the bond angle Zr-S-Zr and the Zr-S disorder.

	XRD at [121]		EXAFS		
	Crystallite size (nm)	Lattice parameters (Å)	Zr-S distance (Å)	Zr-S-Zr bond angle (°)	Zr-S disorder σ^2 (Å^2)
Powder	43 ± 6	a = 7.0533 b = 9.9725 c = 7.0730	2.539 ± 0.004	144.6 ± 2.8	0.0059 ± 5x10^{-4}
Thin film	22 ± 1	a = 7.0511 b = 9.9569 c = 7.0479	2.546 ± 0.006	146.8 ±1.6	0.0066 ± 3.1x10^{-4}

disorder for Zr-S bonds, is ~ 0.006 $Å^2$, which is rather low and suggestive of high crystallinity of the $BaZrS_3$ powder. A lower variance of the Zr-S bond distance is estimated for the powder as compared to the film.

Overall, we find the parameters in Table 1 to be rather comparable, except for the higher crystallinity of the powder, as evidenced by the bigger crystallite size from the XRD peak and lower σ^2 for Zr-S bond for the powder as compared to the film. Nonetheless, this comparison confirms the good quality of the thin film. The average crystallite size for powder is still small, indicative of the rather high activation energy barrier for $BaZrS_3$ formation and growth of crystallites, i.e., single domains. A longer thermal process, instead, facilitates several such domains to join along the crystallite boundaries and form large polycrystalline grains instead of forming larger crystallites. Whereas in the films, a rapid annealing limits this process to a much smaller grain size.

Electronic Structure

I. Core level photoelectron spectroscopy

Figure 2 shows survey scans measured for the bare indium foil and $BaZrS_3$ powder on In foil and $BaZrS_3$ thin film, collected using the different photon energy sources. All three surveys on $BaZrS_3$ show core level peaks from Ba, Zr, S, O and C, while the low photon energy survey spectrum of $BaZrS_3$ powder contains in addition the peaks of In. The substrate signals still do not interfere with the main core levels of interest from $BaZrS_3$ sample (Ba 3d, Zr 3p, S 2p and Zr 3d), which remain distinctively visible. Overlap between signals originating from the $BaZrS_3$ sample and In foil occurs for O 1s, C 1s and the valence band spectrum. Consequently, the valence band spectrum of the low photon energy measurement of the powder was obtained by subtracting the valence band spectrum of the bare In foil. The survey scans for both samples, measured with Ga K_α, exhibit as well signatures of all relevant core levels with a clear O 1s signal, but no clear C 1s signal. The probing depth with Ga K_α, is therefore high enough, in both powder and thin film samples, to suppress the signal coming from adventitious C at the sample surface, whereas the presence of O is detected further into the material.

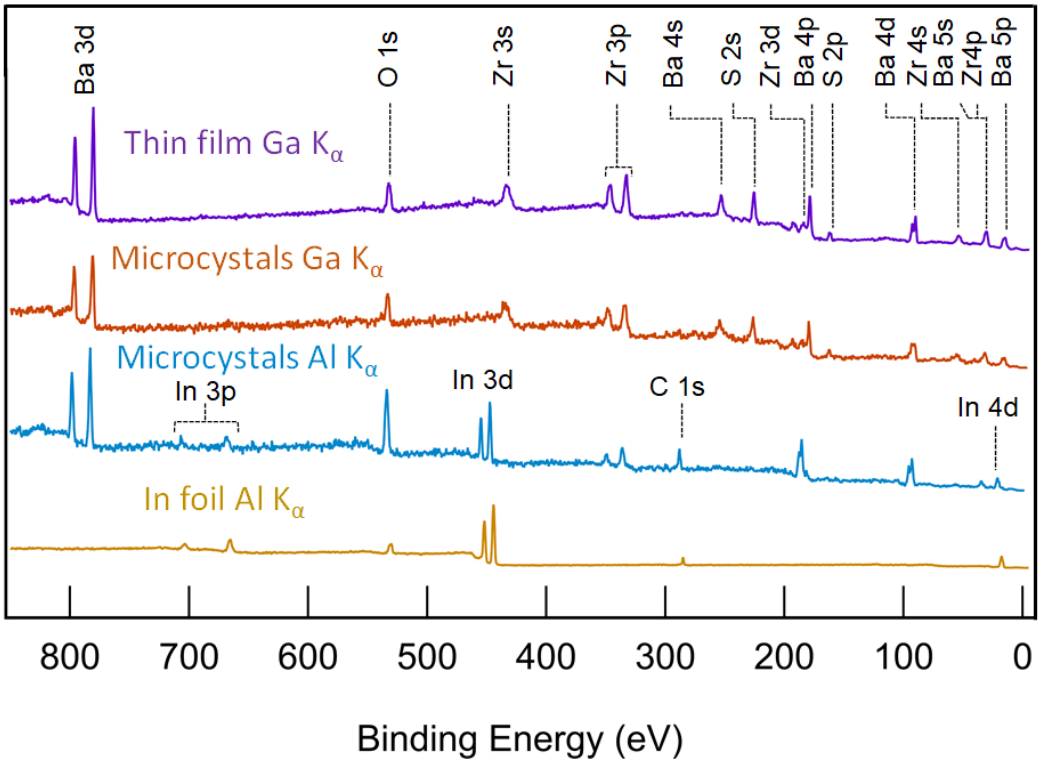

Figure 2: Photoelectron spectroscopy surveys measured with Al K_α and Ga K_α of the $BaZrS_3$ powder (blue, orange) and thin film (purple). As comparison, the survey of Indium foil measured with Al K_α is reported (yellow).

Fig. 3 shows the core levels of Ba 3d, Zr 3p, S 2p for the powder sample at low – Al K_α (Fig. 3a) and high – Ga K_α – photon energies (Fig. 3b), and for the thin film sample at Ga K_α (Fig. 3c). In addition, the corresponding Zr 3d core level is shown for the powder at low photon energy (Fig. 3a top right panel), while the O 1s core level is shown for the high photon energy measurements of both systems (Fig. 3(b,c) middle and bottom right panels). The Ba 3d peaks can be fitted with one spin-orbit split state with fixed intensity ratio of 3:2 for all measurements and with the spin orbit splitting energy of about 15.3 eV, consistent with the value of 15.33 eV reported in the literature.[35,36] The binding energy of Ba $3d_{5/2}$ is 780.50 eV for both the powder and thin film samples when measured for Ga K_α, while a value of 781.10 eV is obtained for the powder when measured using Al K_α. The Ba 3d peak widths for the spin-orbit split states is 2.13 eV and 1.96 eV for the powder and the thin film sample, respectively,

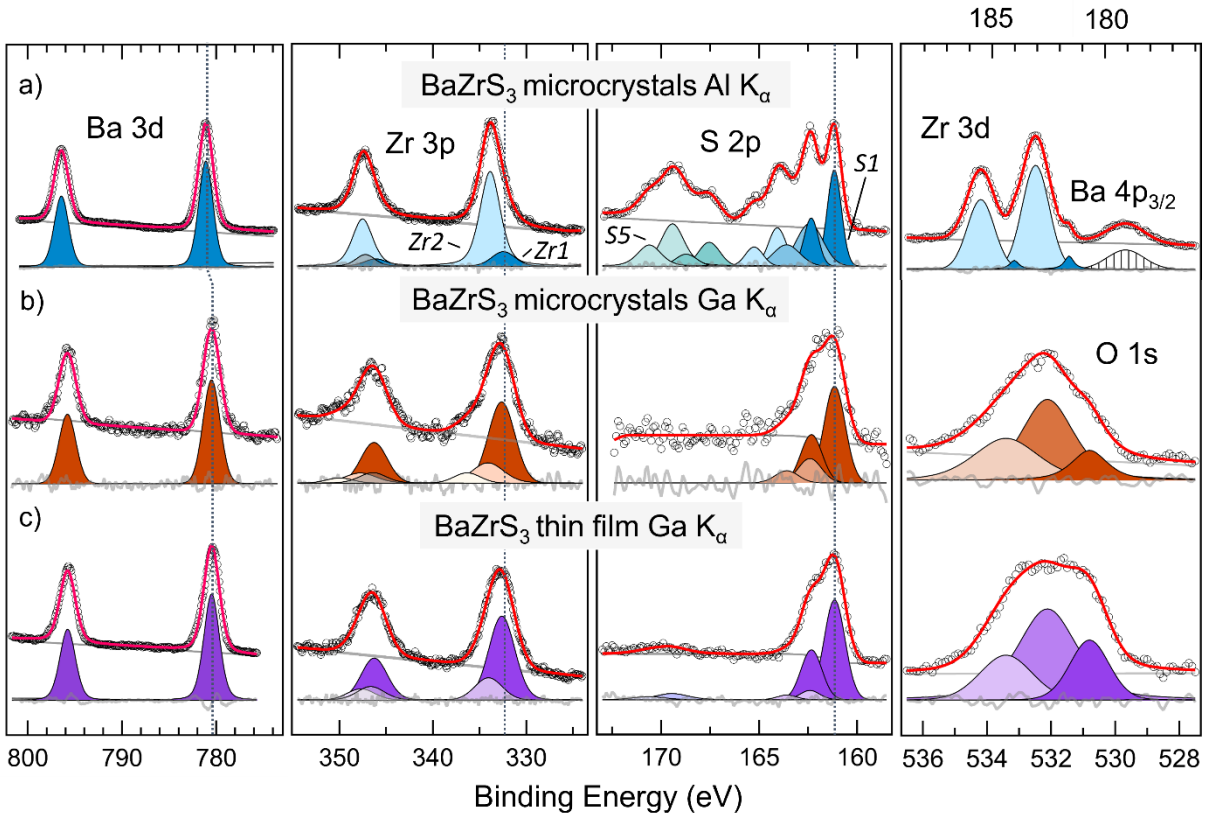

Figure 3: XPS spectra of Ba 3d, Zr 3p, S 2p and Zr 3d or O 1s measured at low photon energy (1.487 keV) and high photon energy (9.25 keV) for the $BaZrS_3$ powder and the thin film. The spectra are energy calibrated vs Fermi of the thin film, with the binding energy of S1 S $2p_{3/2}$ at 161.15 eV. (a) Low photon energy XPS spectra of the core levels of the $BaZrS_3$ powder. (b) High photon energy XPS spectra for the $BaZrS_3$ powder. (c) High photon energy XPS spectra of core levels of the $BaZrS_3$ thin film.

for Ga K_α, while the value is slightly lower, 1.80 eV, for the powder by Al K_α. The difference in large part is accounted for by the contribution to the resolution expected from the different pass energies used for these measurements (see *Experimental Section)*.

Two distinct contributions to the Zr 3d peaks are discernible with the Zr $3d_{5/2}$ components occurring at 181.60 eV and 183.08 eV when measuring the powder using Al K_α. For Ga K_α (Fig. 3b and 3c), the peaks of Zr 3d (185-180 eV) suffer from the higher noise level in the signal resulting from the lower cross-section of Zr 3d compared to Ba $4p_{3/2}$, and the complex structure of satellite peaks instead of the sharp Ba $4p_{1/2}$ peak[37]. For this reason, the chemical environment of zirconium was mainly investigated through the core level Zr 3p at high photon energy. For the three measurements of Zr 3p, the fits were executed by constraining the binding energy separation value between the chemical species to be the same for all the spectra and aligning the peak positions at the same binding energy. Additionally, the Zr $3p_{1/2}$ and Zr $3p_{3/2}$ peaks were deconvoluted by keeping the energy difference to be 13.66 eV and fixing the intensity ratio as 2:1, defined by the spin-orbit splitting. A background peak (in Fig. 3 in grey) caused by a shake-up transition was also considered for determining the correct intensity ratio[38].

For the measurements at Al K_α, Zr $3p_{3/2}$ peaks positions are obtained at 332.44 eV (which we call *Zr1*) and 333.86 eV (*Zr2*), with an energy difference (Zr $3d_{5/2}$ - Zr $3p_{3/2}$) of 150.8 eV for both species. For this photon energy, the FWHM is 2.9 eV for *Zr1* and 2.6 eV for *Zr2*. The corresponding Ga K_α spectra show Zr $3p_{3/2}$ peaks at 332.64 eV and 334.11 eV for the powder, and at 332.62 eV (*Zr1*) and 334.05 eV (*Zr2*) for the thin film, respectively. In addition, the powder presents a third peak of Zr $3p_{3/2}$ at 336.33 eV. The widths for Zr $3p_{3/2}$ peaks are 3.3 eV for *Zr1* and 4.0 eV for *Zr2* at Ga K_α for the powder, and 3.3 eV (*Zr1*) and 3.4 eV (*Zr2*) for the thin film. Focusing on the two common zirconium species *Zr1* and *Zr2*, we notice that their relative intensity changes on probing from low to high photon energies: with Al K_α, the predominant species is *Zr2*, while with Ga K_α *Zr1* becomes more intense. Considering that the probing depth of the XPS increases from a few nm with Al K_α to 10-15 nm with Ga K_α, we can expect that *Zr2* is the oxidized zirconium present in the surface region (probably ZrO_2 or $BaZrO_3$), and *Zr1* can be likely assigned to the perovskite structure $BaZrS_3$ in the bulk.

Our microscopy studies [7] support the presence of zirconium oxide species in the thin film, even when measured with Ga K_α. From the STEM analysis of the thin film combined with the

elemental map distribution, we notice that the oxygen-rich phases are linked to the zirconium-rich phases, indicating the dispersion of amorphous Zr-O species throughout the bulk of the sample. Such secondary phases could form during the nucleation of the $BaZrS_3$ grains that leads to the aggregation of O around Zr, a process also aided by the presence of pinholes and cracks in the thin film. In contrast, the powder is fabricated in a sealed ampoule, and it is less likely that oxygen atoms are absorbed from the atmosphere during the heating process. Rather, a more plausible scenario is that some oxygen is trapped in the sealed ampoule and therefore reacts during annealing, or the oxidation process occurs after exposure to ambient conditions.

As clearly observed in Fig. 3, the S 2p spectrum exhibits a multi-component structure, ranging from two to five (from *S1* with the lowest binding energy peak to *S5* with the highest binding energy peak) distinguishable components. The most complex and resolved S 2p spectrum of the Al K_α was deconvoluted, and then the results were subsequently employed to fit the Ga K_α S 2p spectra. During the fitting procedure, the intensity ratio of the S $2p_{3/2}$ and S $2p_{1/2}$ was maintained to be 2:1, and the S 2p peaks splitting was set to 1.18 eV. The high complexity of S 2p peaks measured at low photon energy can be associated to a varied chemical environment of the sulfur within the film surface region. From the fit, the component S $2p_{3/2}$ corresponding to *S1* is observed at 161.15 eV, while components *S2* and *S3* appear at 162.41 eV and 164.06 eV, respectively. Two more distinct states *S4* and *S5* can be observed at 167.55 eV and 169.41 eV, which can be attributed to the oxidized sulfur compounds of $BaSO_3$ and $BaSO_4$ [39]. The results from the high photon energy, which probes deeper into the sample, can also be fit with an S1 and S2 having the same shift, for both the powder and the thin film samples, i.e. S $2p_{3/2}$ of *S1* the to be at 161.15 eV and *S2* at 162.41 eV. In the case of the thin film (Fig. 3c), an adventitious sulfur component linked to sulphate is found at 169.46 eV. As for the other core levels, the S 2p peaks measured using the Al K_α source show narrower features than the ones measured by the Ga K_α radiation, due to the experimental requirement of a higher pass energy to compensate for the lower core level photoemission intensity when using the Ga K_α source. This explains why at Al K_α, the lowest binding energy peak shows a FWHM of 0.84 eV, while at Ga K_α the FWHM is ~ 1.2 eV for both the measurements of the powder and the thin film. Unlike the zirconium features, the sulfur peaks of the powder show stronger dynamicity when the probing depths increases with the hard X-rays in XPS. In fact,

from a five-species manifold of sulfur at Al K_α, only two signatures could be detected with the Ga K_α source. As indicated previously, S 2p peaks can be classified into two sub-groups: the higher binding energy peaks related to the sulfur oxides (172 – 166 eV), and the lower binding energy peaks (165 - 161 eV). Some validation of the oxide species is given by the binding energy difference Ba $3d_{5/2}$ – *S5* S $2p_{3/2}$ of 611.69 eV, comparable to the literature value of 611.5 eV for the barium sulfate $BaSO_4$[39]. The lower energy sulfur peaks *S4* in orange is assigned to the barium sulfite $BaSO_3$, where Ba $3d_{5/2}$ – S4 S $2p_{3/2}$ is 613.55 eV. The binding energy difference between the *S5* and *S4* S $2p_{3/2}$ is ~1.9 eV, consistent to the difference expected for sulfate – sulfite species[40]. One can clearly observe that the *S3* and *S2* signals decrease in intensity relative to S1 when comparing measurements with soft X-rays and hard X-rays. This observation hints both *S2* and *S3* featured to be related to surface terminated sulfurs, with *S3* from the bonds S-C or S-H and *S2* from the Ba-Zr-S-C[41]. Finally, the *S1* peak corresponding to the lowest binding energy one in the S 2p spectra appear for all the three measurements, showing higher intensity with higher probing energy, suggesting their close relation to the sulfur peak of the perovskite structure $BaZrS_3$.

O 1s was measured for the powder and the thin film at high photon energy. In both cases the data were fitted with three peaks at 530.80 eV, 532.11 eV and 533.41 eV, respectively assigned to Zr bound to O, $BaSO_4$ and chemisorbed O, with the proportion of the different O species being different between the powder and the thin film. Similar results were obtained in the paper by Mukherjee *et al*. [18], where the varying ratios of the chemical species obtained at different annealing temperatures could be attributed to the varied surface oxidation effects.

A range of O products are observed into the material up to 15 nm, as confirmed by the presence of sulfur oxides and a Zr-O-rich phase (shown in Fig. 3), consistent with our previous observations, as well as by Ramandan *et al.* via EDX elemental maps[12]. For both samples, we notice that the oxide species are distributed differently along the depth: the sulfur oxides $BaSO_3$ and $BaSO_4$ are limited to the first 1-2 nanometers of the surface, while the Zr-O species extend deeper than 10 nm from the sample-air interface. The oxidation variability within the first 10 nm of the perovskite surface might be deleterious to the case of device integration process because of the high resistance of the oxide compounds.

In contrast to sulfur and the zirconium spectra, the Ba 3d spectra do not reveal specific changes in the bonding environment, assuming a predominant oxidation state +2, which

includes contributions from chemical species besides the perovskite. However, considering *S1* as the perovskite peak at the same binding energy for all three sets of measurements, the position of Ba $3d_{5/2}$ occurs at slightly different values: 781.10 eV for Al K_α, and at 780.50 for Ga K_α. At high photon energy, the XPS measurements reveal a diminished presence of mixed compound species (e.g., $BaSO_4$) than the Al K_α, which may contribute to the shift of the Ba $3d_{5/2}$ peak towards lower binding energy values. Other oxidation compounds involving barium, such as BaO_2, cannot be ruled out. Fig. 6a reports a schematic view of the $BaZrS_3$ surfaces, as investigated in this paper.

Differently from the powder sample where energy calibration was performed internally and only relative energy differences could be considered, for the thin film all the peaks were energy-calibrated according to the Au $4f_{7/2}$ peak position at 84.0 eV. Table 2 reports the peak positions of selected core levels representative of all the elements present in $BaZrS_3$, where the lowest binding energy peaks of *Zr1* Zr $3p_{3/2}$ and *S1* S $2p_{3/2}$ are listed.

Table 2: Peak positions for the $BaZrS_3$ thin film measured at Ga K_α, calibrated against the Fermi level.

	Ba $3d_{5/2}$ (eV)	**Zr1 Zr $3p_{3/2}$ (eV)**	**S1 S $2p_{3/2}$ (eV)**
Binding Energy vs Fermi	780.50	332.62	161.15

Table 3 reports the binding energy difference between the peaks of Ba $3d_{5/2}$, *Zr1* Zr $3p_{3/2}$ and *S1* S $2p_{3/2}$, based on the peak positions obtained from the fits, and compares the values for both powder and thin film, collected at Al K_α and Ga K_α. We notice that the energy differences between the peaks collected at Ga K_α are rather similar and within the experimental uncertainty limits. This observation can be extended to the case of Al K_α for the offset between Zr and S, with the exception of the values accounting for the Ba $3d_{5/2}$ which resides at higher binding energy values when measured with Al K_α. Those findings are in agreement with our previous photoemission report on surfaces of $BaZrS_3$ thin films[18] . Averaging the offset values *Zr1 - S1* for all the measurements reported in Tab. 3, the mean binding energy difference (Zr1 $3p_{3/2}$ – S1 $2p_{3/2}$) for the $BaZrS_3$ perovskite amounts to 171.42 eV.

Table 3: Binding energy difference between the barium, zirconium and sulfur peaks for our model systems of $BaZrS_3$, calculated from the fitted peak positions of Ba $3d_{5/2}$, and the lowest binding energy peaks position of Zr1 Zr $3p_{3/2}$ and S1 S $2p_{3/2}$ for the three XPS investigated cases.

	Ba $3d_{5/2}$ – S1 $2p_{3/2}$ (eV)	**Zr1 $3p_{3/2}$ – S1 S $2p_{3/2}$ (eV)**	**Ba $3d_{5/2}$ – Zr1 Zr $3p_{3/2}$ (eV)**
Al K_α XPS – powder	619.95	171.29	448.66
Ga K_α XPS - powder	619.35	171.49	447.86
Ga K_α XPS - thin film	619.35	171.49	447.88

Table 4: Composition of the powder and the thin film sample, expressed as ratios of elemental concentrations from EDX and XPS techniques. *the compositional ratio is not applicable.

	[Ba]/([Ba]+[Zr])	**[S]/ ([Ba]+[Zr]+[S])**	**[O]/ ([Ba]+[Zr]+[S]+[O])**	**[S]/([S]+[O])**
EDX - powder	0.52	0.55	0.08	0.86
Al K_α XPS – powder	0.29	0.23	N/A*	N/A*
Ga K_α XPS - powder	0.58	0.49	0.42	0.41
EDX - thin film	0.50	0.54	0.08	0.86
Ga K_α XPS - thin film	0.57	0.48	0.31	0.52
Stoichiometric	0.50	0.60	0.00	1.00

Table 4 provides elemental composition analyses obtained from our photoemission measurements performed for the powder and thin films, in comparison to the atomic percentages given by EDX data. The elemental composition from the XPS spectra was obtained through the sum of the areas of all the fitted peaks of Ba $3d_{5/2}$, Zr $3p_{3/2}$, S $2p_{3/2}$ and O 1s weighted on their cross section at 9.25 keV (the calculation of the cross sections at 9.25 keV is reported in the Supplementary Information), and taking into account the number of sweeps and the acquisition time. It is interesting to note that the EDX compositional analyses on the

thin film and the powder match, although the synthesis processes are completely different. The presence of O in the bulk of the thin film can be explained by the ToF-ERDA measurements by Comparotto et al[7], where the first few nanometers of the thin film surface are oxidized and the bulk contains clusters of amorphous Zr-O, which are not captured by XRD. Also, the high susceptibility of $BaZrS_3$ towards surface oxidation may be further aided by the rapid thermal process that generates cracks and pin-holes, allowing larger access for atmospheric O_2 to react with the film. In the powder, the presence of atomic O is not clearly unraveled, coming either only from the surface or also from the bulk. The dissimilarity in the values reported by EDX and the XPS analysis for both samples is significant. This is not surprising, considering the appreciably higher bulk sensitivity of EDX, probing up to several micrometers into the material, while XPS probes only the first few nm from the material surface. When the composition is evaluated by XPS (Tab. 5), the atomic percentage reveal the partial substitution of the sulfur by the oxygen which for the powder sample the ratio O/S is 1.45, while for the thin film is 0.94. This is in sharp contrast to the much lower O/S ratio (around 0.16) for both powder and films obtained from the EDX data, demonstrating that the oxygen is mainly present in the surface layer for more than 10 nm, and the true perovskite without impurities resides only deeper in the sample. The elemental estimation from spectroscopy displays a lower concentration of S ([S]/([Ba]+[Zr]+[S) < 0.6) compared to the EDX analysis. This is primarily related to S being substituted by O (i.e. [S]/[S]+[O] < 1), an effect that is dominant in the first ten of nanometers of the surface. We note here that replacement of S by O simply refers to undesired surface reactions, and not necessarily random anionic site substitution of S by O in from $BaZrS_3$ lattice, as already negated by our previously published structural data[18]. Probing by XPS from low to high photon energy for the powder sample, the ratio ([Ba]/(Ba]+[Zr]) increases and gets closer to the stoichiometric value, and [S]/([Ba]+[Zr]+[S]) approaches the EDX value. Irrespective of the relative amount of the atomic species, at high photon energy the spectra of Ba 3d, Zr 3p and S 2p overlap completely (Fig. 3), indicating that regardless of the fabrication technique, oxidation is difficult to avoid and that both synthesis procedures form the same superficial species. For this reason, before proceeding to interface fabrication of device structures with the pure $BaZrS_3$, it is necessary to clean the surface (at least 10 nm) of $BaZrS_3$ samples. This may be done with chemical or physical methods that remove the adventitious species, or by having a better control of the surface reactivity during synthesis.

II. Valence Band Photoemission and DFT calculations

Another crucial feature of the electronic structure that can be studied and compared among the samples is the valence band, that contains information about the density of states of the hybridized orbitals for a given system, consequently defining the samples' properties. The valence band spectra for the two systems are shown in Fig. 4: the powder with Al K_α (in blue), and the valence bands acquired by hard X-rays for the powder (in orange) and for the thin film (in purple). In the figure, the three valence bands were normalized to the main feature at around 5 eV and energy calibrated vs Fermi level of the thin film, as described in the *Experimental Section*. Qualitatively, the measurements acquired at high photon energy exhibit the same shoulder between 0 and 4 eV, and they have a narrow feature around 5 eV. On the other hand, the valence band spectrum measured with lower photon energy shows similar, albeit broader features, where the low binding energy shoulder has smaller intensity and the feature at 5 eV prevails in the valence band spectrum.

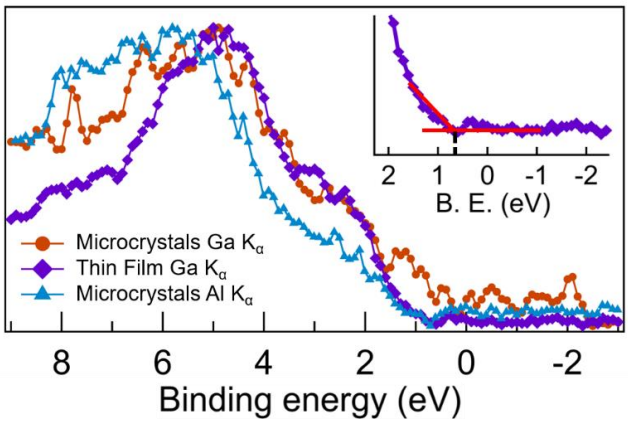

Figure 4: Comparison of the valence bands acquired for powder obtained with Al K_a photon energy (▲), Ga K_α photon energy (●), and for the thin film with Ga K_α photon energy (♦). All the spectra are calibrated through the S $2p_{3/2}$ at 161.15 eV. Intensities are normalized for comparison. Inset: zoom on the valence band edge for the determination of the VBM.

Fig. 5a shows the orbital-resolved projected density of states of the $BaZrS_3$ matrix obtained from DFT calculations, displayed to the valence band maximum at energy 0 eV, which allows us to identify the orbital contributions of the different constituent elements of $BaZrS_3$ in the valence band. It can be clearly seen that the theoretical DOS in the range 0 - 5 eV results predominantly from the 3p states of the S atoms and 4d states of the Zr atoms, in accordance with previous reports[6,16,42]. Moving to the energy range 10 - 15 eV, the total DOS results from

the hybridization of the p-states of barium with the s-states of sulfur, explaining the difficulty to fit the peaks with the 2:1 ratio for the intensity of Ba 5p in the experimental spectra. It is clear from the DFT calculations that the band edges are populated primarily by contributions from the orbitals of Zr and S, facilitating optical transition between the S 3p states in the valence band to the transition metal d states in the conduction state, and consequently, leading to a strong band edge light absorption. The orbitals of Ba, on the other hand, are more deep-seated in energies. This follows from the perovskite structure, where Ba resides at the A-site assuming a larger cuboctahedral volume (Ba-S_{12}, i.e. with 12 sulfur atoms) and consequently showing weaker hybridization effects compared to a much smaller Zr-S_6 octahedral volume. Some minor mixing of Ba states is promoted by a larger spatial distribution of Ba atoms in orthorhombic symmetry, with Zr-Ba interatomic distances spanning from 4.08 – 4.39 Å as extracted from EXAFS analysis, which has insignificant effect on light absorption. The population of Zr d orbitals in the lowest energy conduction bands and chalcogen p orbitals in the highest energy valence bands, both would be sensitive to the degree of cooperatively

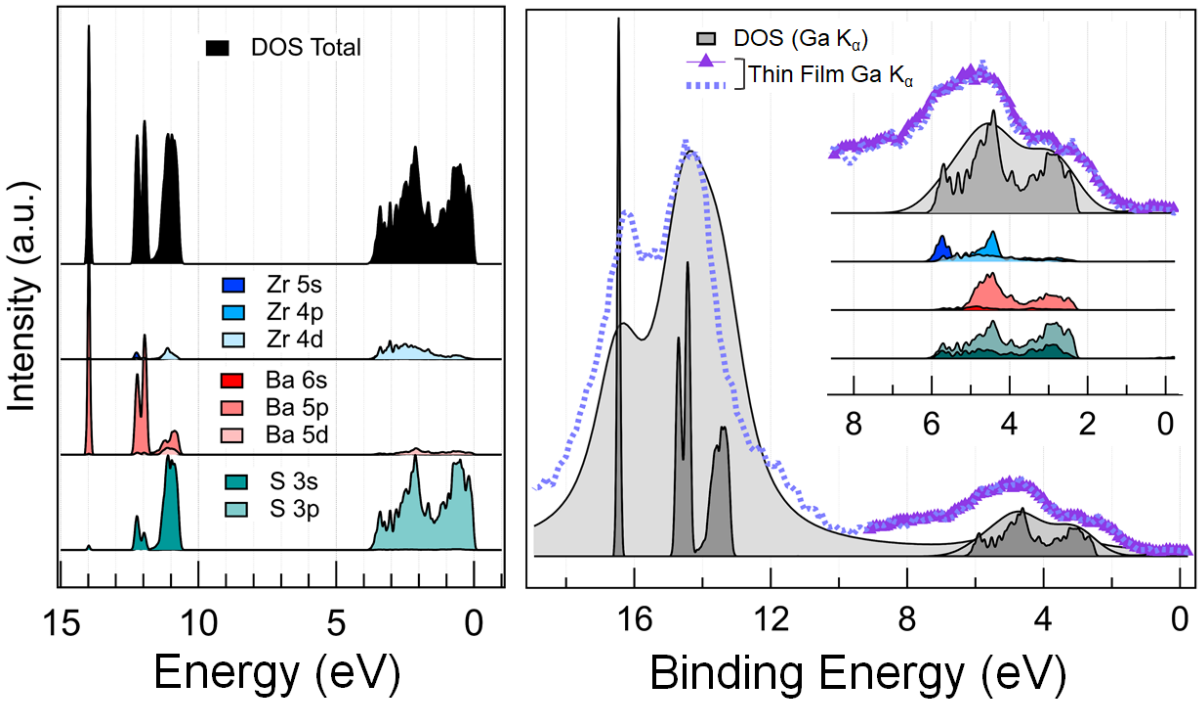

Figure 5: Theoretical density of states, compared to the experimental valence band by XPS. (a) Orbital-resolved projected density of states for the $BaZrS_3$ matrix. (b) Comparison of the experimental valence bands of thin film sample (photon energy: 9.25 keV) with the theoretical contributions of single atoms, weighted by the cross sections at 9.25 keV. The density of states in (b) are energy calibrated by Au $4f_{7/2}$ at 84.0 eV.

tilting of adjacent Zr-S_6 (i.e. with 6 sulfur atoms) units along the three crystallographic axes. Our EXAFS analysis indeed reveals distorted Zr-S-Zr bond angles of 144 - 147° in case of both powder and thin film. These octahedral rotations bring adjacent Zr sites closer, lowering the orbital integral and consequently narrower bands. Notably, the conduction band also includes some contributions from S 3d states, expected from Zr-S bonds having some covalent character. The interplay between Zr-S covalency and Zr-S-Zr angles are crucial factors that determine the band gap of $BaZrS_3$ to be ~ 1.7 – 1.8 eV, making it a semiconductor, unlike the chalcogenide analogue $BaZrO_3$, where higher ionicity of Zr-O bonds affects less hybridization and widening the gap to 3.9 eV[42].

In order to compare the calculated DOS with the XPS spectra, the DOS needs to be weighted by the orbital cross section for the probing XPS energy. The valence band of $BaZrS_3$ measured at Al K_α (Fig. S2) reproduces the theoretical DOS quite well. In the present study, we focus on the valence band spectrum recorded with Ga K_α due to the suppressed surface contributions, rather than the Al K_α measurements. Therefore, Fig. 5b reports the theoretical DOS weighted by the XPS cross section for an energy of Ga K_α, as compared to the experimental spectra. From Fig. 5b we notice that the valence band features acquired at Ga K_α contains the contributions from all the perovskite atoms. In particular, the Ba 5p states are enhanced compared to the S 3p and Zr 4d, making the low binding energy shoulder (at around 2 eV) attain comparable intensity as the one at 5 eV. Applying Lorentzian and Gaussian broadening to the theoretical results, the two features evolve into the displayed grey area, gaining an overall similarity to our experimentally obtained valence band spectrum at Ga K_α, both for the thin film and the powder.

With respect to the theoretical DOS weighted to the cross sections, the valence band spectra show generally broader features and a higher background, which can be explained by scattering effects in the photoemission process, as well as the presence of mixed compounds and impurity atoms. As seen in the theoretical results, the states of S and Zr contribute to the valence band shape, as displayed when $BaZrS_3$ samples are measured for soft and hard X-rays. From our core level measurements of S 2p and Zr 3p shown in Fig. 3, we noticed the presence of mixed compounds attributed to Zr-O and Ba-S-O residing in the first 1-2 nm of the surface, and hence evidenced especially when measured with Al K_α radiation. Their presence is most probably reflected in the broadening of the valence band spectra at higher energy shifted

some eVs from the Fermi level and up to 7 eV, with the addition of the oxygen feature noticeable by the peak at around 7 eV, corresponding to the O 2p (Fig. 5 and S2)[43,44]. On the other hand, the valence band spectra measured at Ga K_α (Fig. 5b) are narrower, in particular for the thin film, confirming the low contribution of undesired species to these spectra.

Determining the valence band maximum relatively to the Fermi level holds significance in the interfacial energetics and in the construction of the energy diagram of materials when put in contact. In our XPS measurements, energy calibration against Fermi was feasible only for the thin film probed by Ga K_α radiation. Using a linear intersection between the valence band edge feature and the baseline, we could determine a VBM to be at 0.7 eV vs Fermi level. The measurements on the crystals were aided by the neutralizer, making it difficult to calibrate the spectra in an appropriate way. Therefore, the measurements for powder were energy calibrated by assigning the S 2p (*S1*) binding energy position at 161.15 eV at all probing energies. Neglecting the valence band of the powder at Ga K_α because of the low signal-to-noise ratio, we notice that the VBM for the powder at Al K_α appears at the same binding energy position as for the Ga K_α spectrum for the thin film (see Fig. 5). From this, we can suggest that

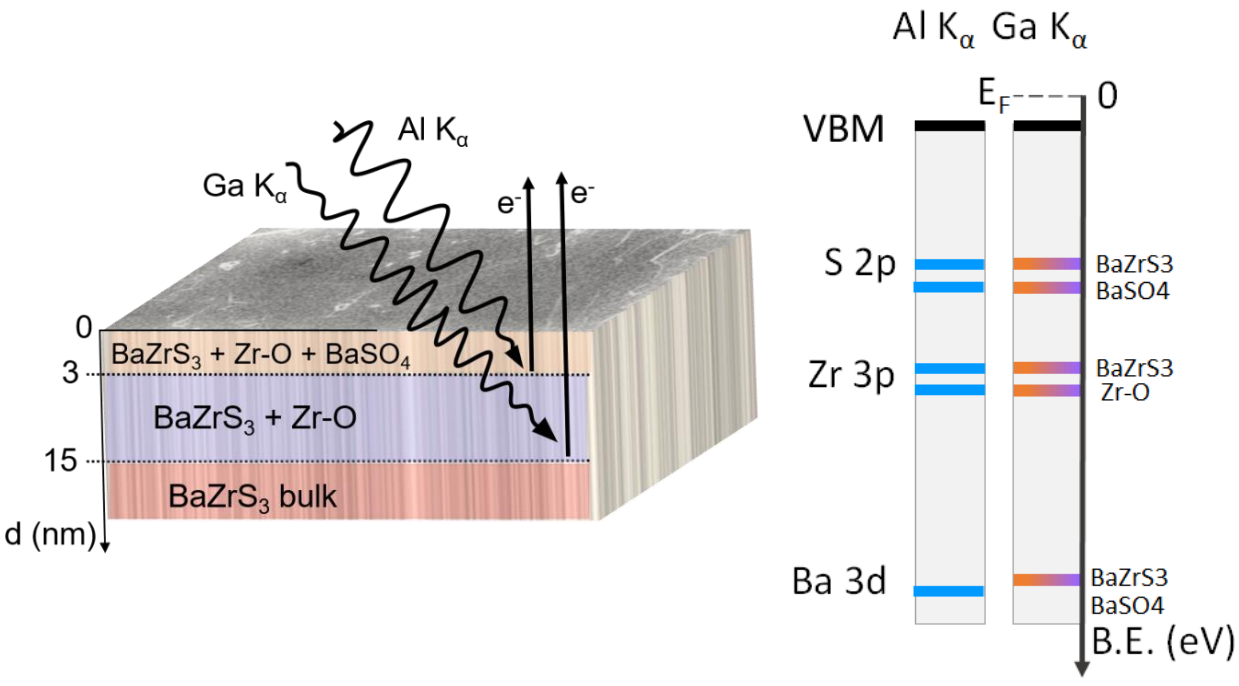

Figure 6: Major findings about (a) phase distributions and (b), core level positions and valence band maxima for $BaZrS_3$ samples measured at Al K_α and Ga K_α radiations. The solid lines represent the core levels binding energy positions (blue for Al K_α and orange-to-purple for Ga K_α) in an increasing binding energy scale with 0 at the Fermi level (E_F).

the oxides compounds do not interfere with the frontier valence band region (from 0 eV to 4 eV) and specifically not with the valence band maximum. These typically large band gap oxides, therefore, seem to coexist with $BaZrS_3$, as opposed to forming alloys and increasing the band gap, and remaining mostly confined to the surface. Fig. 6b represents schematically the results from the XPS analysis, for Al K_α and Ga K_α. In the figure, the core levels are represented by solid lines (blue for Al K_α and an orange-purple gradient for Ga K_α) in an increasing binding energy scale with 0 at the Fermi level (E_F). As discussed earlier, the S and Zr peaks at Al K_α and Ga K_α are at the same binding energy position, with the exception of Ba 3d.

The position of the VBM relative to the Fermi level determines the type of a given semiconductor. Considering the band gap of 1.84 eV as given by the bulk photoluminescence in the previous work for this specific thin film [7], the valence band measurements indicate that the Fermi level is closer to the VBM, rather than to the conduction band, therefore suggesting weak p-type doping. This approach highlights the importance of proper identification of all core-level spectra and the valence band to arrive at a comprehensive understanding of electronic structure of $BaZrS_3$, and determining the type of semiconductor achieved through different synthesis strategies.

Conclusions

Our study concerns the investigation of chalcogenide perovskites $BaZrS_3$ samples in the form of powder and thin film with regard to their electronic structure. After ensuring good material quality of both systems in terms of geometric structure and stoichiometry, we focused on the study of the surface composition by photoelectron spectroscopy with the two photon energies Al K_α and Ga K_α, validating the material chemistry at different probing depths. The more bulk sensitive Ga K_α measurements on the two samples reveal a significant resemblance in the chemical environments, while the more surface sensitive Al K_α on the powder shows stronger signals from oxidation species. For all the XPS measurements, only one main peak of Ba 3d could be resolved, obscuring the detailed chemistry of the barium atom. Conversely, the analysis of the zirconium and sulfur spectra reveals that the oxides related to zirconium extend more than 10 nm towards the bulk of the samples, while oxysulfide compounds are confined only to the first 1-2 nm. Except for the persistent surface oxidation effects, the $BaZrS_3$ spectra measured with Ga K_α source on both sample types were cleaner and allowed us to identify the

peaks of the $BaZrS_3$ matrix. The spectra of valence bands measured matched well with the theoretical DOS, substantiating how bond characteristics are strongly related to the orthorhombic structure maintained through the angular -Zr-S-Zr- inorganic network. At high photon energy, we find the valence band spectra to be contributed strongly by the energy levels of all atoms S, Zr, and Ba, enhanced by the higher cross section from the photoelectric process. Finally, our analysis on the valence band maximum indicates that the presence of the oxides does not contribute to the position of the valence band maximum. Herein, we achieve a relevant insight to electronic landscape of $BaZrS_3$, and such strategy could be extended to other members of the chalcogenide perovskite group to harness their full potential as photovoltaic materials.

Acknowledgments

The authors gratefully acknowledge STandUP for Energy, the Swedish Research Council (2018-06465, 2018-04330, 2022-06076 and 2023-05072), Swedish Energy Agency (P50626-1) and the Wallenberg Initiative Materials Science for Sustainability (WISE) funded by the Knut and Alice Wallenberg Foundation (KAW) for financial support. J.S., C.C. and G. A. gratefully acknowledge STandUP for Energy, the Swedish Research Council (2017-04336) and the Swedish Energy Agency (project 52483-1) for funding this research, as well as Myfab Uppsala for providing facilities and experimental support. Myfab is funded by the Swedish Research Council as a national research infrastructure. S.M.B acknowledges the support from the Swedish Research Council (research grant 2018-05525). We acknowledge DESY (Hamburg, Germany), a member of the Helmholtz Association HGF, for the provision of experimental facilities. Parts of this research were carried out at PETRA III and we would like to thank Aleksandr Kalinko and Maria Naumova for assistance in using P64. Beamtime was allocated for proposal I-20230612 EC. M.A.H. expresses gratitude to Boyang Zhao and Jayakanth Ravichandran for engaging in a fruitful discussion and acknowledges the support received from the VR starting grant 2018-05339.

ASSOCIATED CONTENT

Supporting Information.

Details about: 1. EXAFS parameters, 2. Powder, 3. Cross sections at 9.25 keV, 4. DOS and experimental valence band at Al K_α.

AUTHOR INFORMATION

Corresponding Author

*hakan.rensmo@physics.uu.se

*mahmoud.hafiez@physics.uu.se

Present Addresses

† Technology Department, ReNew Private Limited, ReNew Hub, Golf Course Road sector 43, Gurgaon, Haryana-122009, India

Author Contributions

The manuscript was written through contributions of all authors. All authors have given approval to the final version of the manuscript.

Notes

The authors declare no competing financial interest.

Bibliography

1. Niu, S. *et al.* Thermal stability study of transition metal perovskite sulfides. *J Mater Res* **33**, 4135–4143 (2018).

2. Perera, S. *et al.* Chalcogenide perovskites - an emerging class of ionic semiconductors. *Nano Energy* **22**, 129–135 (2016).

3. Gross, N. *et al.* Stability and Band-Gap Tuning of the Chalcogenide Perovskite BaZrS3 in Raman and Optical Investigations at High Pressures. *Phys Rev Appl* **8**, (2017).

4. Sopiha, K. V., Comparotto, C., Márquez, J. A. & Scragg, J. J. S. Chalcogenide Perovskites: Tantalizing Prospects, Challenging Materials. *Adv Opt Mater* 2101704 (2021) doi:10.1002/adom.202101704.

5. Wei, X. *et al.* Realization of BaZrS3 chalcogenide perovskite thin films for optoelectronics. *Nano Energy* **68**, (2020).

6. Nishigaki, Y. *et al.* Extraordinary Strong Band-Edge Absorption in Distorted Chalcogenide Perovskites. *Solar RRL* **4**, (2020).

7. Comparotto, C. *et al.* Chalcogenide Perovskite BaZrS3: Thin Film Growth by Sputtering and Rapid Thermal Processing. *ACS Appl Energy Mater* **3**, 2762–2770 (2020).

8. Comparotto, C., Ström, P., Donzel-Gargand, O., Kubart, T. & Scragg, J. J. S. Synthesis of BaZrS3Perovskite Thin Films at a Moderate Temperature on Conductive Substrates. *ACS Appl Energy Mater* (2022) doi:10.1021/acsaem.2c00704.

9. Sadeghi, I. *et al.* Making BaZrS3 Chalcogenide Perovskite Thin Films by Molecular Beam Epitaxy. *Adv Funct Mater* **31**, (2021).

10. Niu, S. *et al.* Crystal growth and structural analysis of perovskite chalcogenide BaZrS3 and Ruddlesden-Popper phase Ba3Zr2S7. *J Mater Res* **34**, 3819–3826 (2019).

11. Márquez, J. A. *et al.* BaZrS3Chalcogenide Perovskite Thin Films by H2S Sulfurization of Oxide Precursors. *Journal of Physical Chemistry Letters* **12**, 2148–2153 (2021).

12. Ramanandan, S. P. *et al.* Understanding the growth mechanism of BaZrS3 chalcogenide perovskite thin films from sulfurized oxide precursors. *JPhys Energy* **5**, (2023).

13. Hanzawa, K., Iimura, S., Hiramatsu, H. & Hosono, H. Material Design of Green-Light-Emitting Semiconductors: Perovskite-Type Sulfide SrHfS3. *J Am Chem Soc* **141**, 5343–5349 (2019).

14. Eya, H. I. & Dzade, N. Y. Density Functional Theory Insights into the Structural, Electronic, Optical, Surface, and Band Alignment Properties of BaZrS3 Chalcogenide Perovskite for Photovoltaics. *ACS Appl Energy Mater* **6**, 5729–5738 (2023).

15. Zitouni, H., Tahiri, N., El Bounagui, O. & Ez-Zahraouy, H. Electronic, optical and transport properties of perovskite BaZrS3 compound doped with Se for photovoltaic applications. *Chem Phys* **538**, (2020).

16. Eya, H. I. & Dzade, N. Y. Density Functional Theory Insights into the Structural, Electronic, Optical, Surface, and Band Alignment Properties of BaZrS3 Chalcogenide Perovskite for Photovoltaics. *ACS Appl Energy Mater* **6**, 5729–5738 (2023).

17. Kullerud, G. *Research Techniques for High Pressure and High Temperature*. (Springer Berlin, Heidelberg, 1971).

18. Mukherjee, S. *et al.* Interplay between Growth Mechanism, Materials Chemistry, and Band Gap Characteristics in Sputtered Thin Films of Chalcogenide Perovskite BaZrS 3 . *ACS Appl Energy Mater* (2023) doi:10.1021/acsaem.3c02075.

19. Caliebe, W. A., Murzin, V., Kalinko, A. & Görlitz, M. High-flux XAFS-beamline P64 at PETRA III. in *AIP Conference Proceedings* vol. 2054 (American Institute of Physics Inc., 2019).

20. Ravel, B. & Newville, M. ATHENA, ARTEMIS, HEPHAESTUS: Data analysis for X-ray absorption spectroscopy using IFEFFIT. in *Journal of Synchrotron Radiation* vol. 12 537–541 (2005).

21. Zabinsky, S. I., Rehr, J. J., Ankudinov, A., Albers, R. C. & Eller, M. J. *Multiple-scattering calculations of x-ray-absorption spectra*. *PHYSICAL REVIEW B* vol. 52 (1994).

22. Giannozzi, P. *et al.* Advanced capabilities for materials modelling with Quantum ESPRESSO. *Journal of Physics Condensed Matter* **29**, (2017).

23. Perdew, J. P., Burke, K. & Ernzerhof, M. *Generalized Gradient Approximation Made Simple*. (1996).

24. Armiento, R. & Kümmel, S. Orbital localization, charge transfer, and band gaps in semilocal density-functional theory. *Phys Rev Lett* **111**, (2013).

25. Lehtola, S., Steigemann, C., Oliveira, M. J. T. & Marques, M. A. L. Recent developments in LIBXC — A comprehensive library of functionals for density functional theory. *SoftwareX* **7**, 1–5 (2018).

26. Hamann, D. R. Optimized norm-conserving Vanderbilt pseudopotentials. *Phys Rev B Condens Matter Mater Phys* **88**, (2013).

27. Scherpelz, P., Govoni, M., Hamada, I. & Galli, G. Implementation and Validation of Fully Relativistic GW Calculations: Spin-Orbit Coupling in Molecules, Nanocrystals, and Solids. *J Chem Theory Comput* **12**, 3523–3544 (2016).

28. Monkhorst, H. J. & Pack, J. D. *Special points for Brillonin-zone integrations**. *NUMBER* vol. 13 (1976).

29. Lelieveld, R. & Ijdo, J. W. Sulphides with the GdFeO 3 Structure. *Acta Cryst.* **B36**, 2223–2226 (1980).

30. Sharma, S. *et al.* Bandgap Tuning in BaZrS3Perovskite Thin Films. *ACS Appl Electron Mater* **3**, 3306–3312 (2021).

31. Yu, Z. *et al.* Chalcogenide perovskite BaZrS3 thin-film electronic and optoelectronic devices by low temperature processing. *Nano Energy* **85**, (2021).

32. Xu, J. *et al.* Enhancing the optical absorption of chalcogenide perovskite BaZrS3 by optimizing the synthesis and post-processing conditions. *J Solid State Chem* **307**, 122872 (2022).

33. Márquez, J. A. *et al.* BaZrS3Chalcogenide Perovskite Thin Films by H2S Sulfurization of Oxide Precursors. *Journal of Physical Chemistry Letters* **12**, 2148–2153 (2021).

34. Han, Y. *et al.* P-type conductive BaZrS3 thin film and its band gap tunning via Ruddlesden-Popper Ba3Zr2S7 and titanium alloying. *Chemical Engineering Journal* **473**, (2023).

35. Moulder, J. F., Stickle, W. F., Sobol, P. E. ’, Bomben, K. D. & Chastain, J. *Handbook of X-ray Photoelectron Spectroscopy - A Reference Book of Standard Spectra for Identification and Interpretation of XPS Data*. (1992).

36. Thomson, A. *et al. X-ray Data Booklet*. (Lawrence Berkley National Laboratory, University of California, Berkley, 2009).

37. Yarzhemskya, V.-G., Teterinb, Y. A., Sosulnikovb, M. I. & Karpov, ". *Dynamic dipolar relaxation in X-ray photoelectron spectra of the Ba4p subshell in barium compounds*. *Journal of Electron Spectroscopy and Related Phenomena* vol. 59 (1992).

38. Bargiela, P. *et al.* Towards a reliable assessment of charging effects during surface analysis: Accurate spectral shapes of ZrO2 and Pd/ZrO2 via X-ray Photoelectron Spectroscopy. *Appl Surf Sci* **566**, (2021).

39. Schmitz, P. J. Characterization of the Surface of BaSO4 Powder by XPS. *Surface Science Spectra* **8**, 195–199 (2001).

40. Castner, D. G., Hinds, K. & Grainger, D. W. *X-ray Photoelectron Spectroscopy Sulfur 2p Study of Organic Thiol and Disulfide Binding Interactions with Gold Surfaces*. https://pubs.acs.org/sharingguidelines (1996).

41. Castner, D. G., Hinds, K. & Grainger, D. W. *X-ray Photoelectron Spectroscopy Sulfur 2p Study of Organic Thiol and Disulfide Binding Interactions with Gold Surfaces*. https://pubs.acs.org/sharingguidelines (1996).

42. Bennett, J. W., Grinberg, I. & Rappe, A. M. Effect of substituting of S for O: The sulfide perovskite BaZrS3 investigated with density functional theory. *Phys Rev B Condens Matter Mater Phys* **79**, (2009).

43. Azdad, Z., Marot, L., Moser, L., Steiner, R. & Meyer, E. Valence band behaviour of zirconium oxide, Photoelectron and Auger spectroscopy study. *Sci Rep* **8**, (2018).

44. Bandis, C., Scudiero, L., Langford, S. C. & Dickinson, J. T. *Photoelectron emission studies of cleaved and excimer laser irradiated single-crystal surfaces of NaNO 3 and NaNO 2*. *Surface Science* vol. 442 www.elsevier.nl/locate/susc (1999).